

Kinetic development of low-temperature propane oxidation in a repetitively-pulsed nanosecond discharge

Zhenyang Li^a, Bo Yin^b, Qifu Lin^a, Yifei Zhu^{b,*}, Yun Wu^{b,c}

^a*Institute of Energy, Hefei Comprehensive National Science Center, Hefei, 230026, China*

^b*National Key Lab of Aerospace Power System and Plasma Technology, Xi'an Jiaotong University, Xi'an, 710049, China*

^c*National Key Lab of Aerospace Power System and Plasma Technology, Airforce Engineering University, Xi'an, 710038, China*

Abstract

The kinetics of plasma assisted low temperature oxidation of $\text{C}_3\text{H}_8/\text{O}_2/\text{Ar}$ mixtures have been studied in a wide specific deposition energy with the help of nanosecond repetitively pulsed discharge. Two types of nanosecond pulsed plasma sources, the nanosecond capillary discharge (nCD) and dielectric barrier discharge (DBD) combined with the synchrotron photoionization mass spectrometry are investigated. The electron impact reaction rate of propane dissociation and some combustion chemical reactions rate constants are updated according to the nCD and DBD experiment results, and uncertainty of the reactions are analyzed in detail. Compared to the existing model, the updated model's prediction accuracy has great improvement in species H_2O , CO , CO_2 , CH_4 , CH_2O , CH_3OH , C_2H_2 , C_2H_4 , C_2H_6 , $\text{C}_2\text{H}_5\text{OH}$, $\text{C}_2\text{H}_5\text{OOH}$, $\text{C}_3\text{H}_4\text{-A}$, $\text{C}_3\text{H}_4\text{-P}$, $\text{C}_2\text{H}_5\text{CHO}$, i- $\text{C}_3\text{H}_7\text{OH}$ and $\text{C}_3\text{H}_7\text{OOH}$. The propane oxidation processes assisted by DBD and nCD were compared under different single pulse deposition energy (SPDE) conditions while maintaining the same total deposition energy. The reduced electric field in nCD is concentrated at 150-200 Td and 450-500 Td, whereas in DBD it ranges from 0-25 Td and 50-250 Td. Notably, SPDE shows minimal influence on the propane oxidation process, which is primarily controlled by total deposition energy and demonstrates little dependence on the discharge type (DBD or nCD).

*Corresponding author.

Email address: yifei.zhu.plasma@gmail.com (Yifei Zhu)

Keywords: Plasma-assisted combustion, Low-temperature oxidation, Propane, Kinetic modeling

Novelty and significance statement

The kinetic of plasma assisted $\text{C}_3\text{H}_8/\text{O}_2/\text{Ar}$ oxidation is developed and studied in a wide specific deposition energy of nanosecond repetitively pulsed discharge. Two types of nanosecond pulsed plasma sources (nCD and DBD) are used to validate the kinetic mechanism. The electron impact reaction rate of propane dissociation and some combustion chemical reactions rate constants are updated according to the nCD and DBD experiment results. The prediction accuracy has great improvement, and uncertainty of the reactions are analyzed in detail. The propane oxidation processes assisted by DBD and nCD were compared, and the propane oxidation processes is primarily controlled by total deposition energy and demonstrates little dependence on the discharge type (DBD or nCD).

Authors contributions

Zhenyang Li: Writing-original draft, Formal analysis, Data curation. Bo Yin: Investigation, Experiment development. Qifu Lin: Investigation, Supervision. Yifei Zhu: Writing-review & editing, Conceptualization. Yun Wu: Funding acquisition, Project administration.

1. Introduction

Non-equilibrium plasma-assisted combustion (PAC) offers an effective approach for controlling ignition in internal combustion engines, industrial burners, and aviation engines, thereby enhancing flame stability, reducing pollutant emissions, and expanding ignition limits [1, 2, 3]. Understanding the detailed mechanism of PAC requires studying the kinetic pathways of PAC and quantifying their reaction rates. The kinetics of non-equilibrium plasma-assisted small molecules like methane have been extensively studied [4, 5, 6, 7, 8].

Propane, as the smallest n-alkane with low-temperature reactivity, serves as a typical molecule for studying the kinetics of large alkanes [9, 10], attracting significant attention from researchers. Adamovich et al. [11] proposed a plasma-assisted propane-air combustion kinetic model, which showed

good agreement with experimental temperature and time-resolved OH density measurements. They further studied the plasma-assisted propane oxidation kinetics in $\text{C}_3\text{H}_8/\text{O}_2/\text{Ar}$ mixtures [12], validated the kinetic model with experiments on alkane small molecule density at different temperatures, and found large discrepancies for C_2H_2 and CH_3CHO . Chen et al. [13] employed molecular beam mass spectrometry with tunable synchrotron vacuum ultraviolet photoionization (SVUV-PIMS) to measure hydrocarbons and oxygenated intermediates during plasma-assisted $\text{C}_3\text{H}_8/\text{O}_2/\text{Ar}$ processes, reporting numerous oxygenated intermediates and establishing a kinetic model. However, significant discrepancies existed between the model predictions and experimental measurements for certain hydrocarbons and intermediates. Ban et al. [14] developed a propane-air plasma combustion mechanism and validated it against OH density measurements from experiments [15] that lacked sufficient validation. Based on the above analysis, current kinetic models still exhibit significant discrepancies with experimental measurements in predicting certain hydrocarbons and oxygenated intermediates. Furthermore, current kinetic models are validated under specific single pulse deposition energies, necessitating further validation under larger deposition energy scales.

To validate the kinetics of the plasma-assisted oxidation process in $\text{C}_3\text{H}_8/\text{O}_2/\text{Ar}$ mixtures under large deposition energy scales, stable discharge characteristics and spatiotemporal uniformity are required in experiments. Fast ionization wave (FIW), a nanosecond capillary discharge at moderate pressures, is characterized by spatiotemporal uniformity of discharge, high reduced electric field, high electron energy, and fast propagation speed [16]. FIW serves as an ideal platform for investigating fundamental plasma processes under various discharge parameters and energy deposition conditions [17, 18, 19, 20, 21, 16, 22]. Due to its uniformity and high energy deposition, FIW is suitable for investigating plasma-assisted fuel cracking and oxidation. FIW has two discharge types depending on the presence or absence of a metal screen. In the absence of a metal screen (referred to as nanosecond capillary discharge, nCD), the discharge propagation pattern shifts from single-direction to dual-direction propagation, improving discharge channel uniformity. Consequently, nCD is particularly suitable for validating the accuracy of $\text{C}_3\text{H}_8/\text{O}_2/\text{Ar}$ plasma combustion mechanisms under varying energy deposition conditions.

In this study, we investigate the mechanism of plasma-assisted low-temperature oxidation of propane using numerical simulations and capillary discharge experiments. Section 2 outlines the numerical model, the kinetic schemes, and

the experimental setups. The validation of the kinetic schemes against capillary discharge experiments and DBD experiments [13] is detailed in Section 3. An uncertain analysis of the kinetic schemes is performed using path analysis in Section 4.1. Section 4.2 compares the differences between nCD and DBD in the process of propane oxidation. Finally, we provide conclusions in Section 5.

2. Experiment and modelling method

2.1. The experiment settings

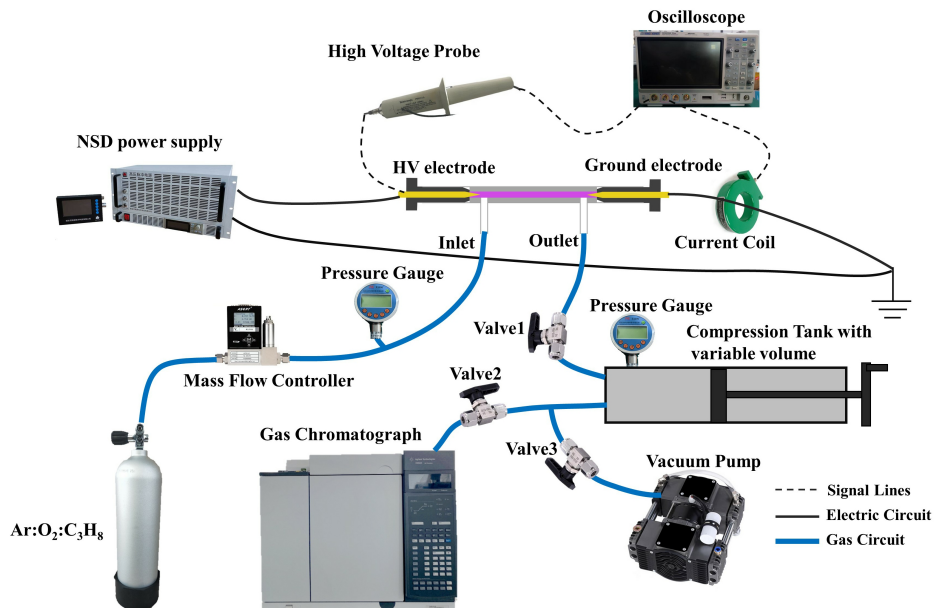


Figure 1: The shematic of the nCD assisted propane oxidation experiment.

The experimental setup of the nCD-assisted propane oxidation is depicted in Figure 1. This setup primarily comprises a gas supply and control system, a plasma discharge system, and a gas collection and analysis system. The discharge system includes a high-voltage electrode, a ground electrode, a quartz tube, and insulating rubber gaskets. The cross-sectional diameter and length of the discharge region are 4.5 mm and 50 mm, and the distance between the two electrodes is 44 mm.

The gas mixture in the cylinder consists of Ar, O₂, and C₃H₈ in a ratio of 92.46:6.33:1.21. The gas flow rate is controlled using a flowmeter (ASERT

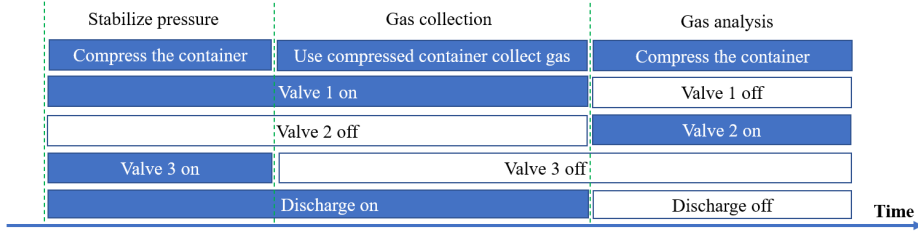


Figure 2: The nCD experimental operation sequence diagram on the process of gas collection.

AST10-ALC 100 sccm) and is set to 30 sccm. Gas flow is controlled using a flowmeter (ASERT AST10-ALC 100 sccm) set at 30 sccm, and pressure is maintained at 3000 Pa by a rotary vane pump, monitored by a vacuum gauge (AILEIKE TT&C Equipment Co., Ltd., ALKC400HJ, 0-1 atm absolute pressure gauge, 0.05%FS). As shown in Fig. 2, valve 3 is adjusted to stabilize the gas pressure before collecting the gas. During collection, valves 3 and 2 are closed, and a compression tank with variable volume stabilizes and stores the low-pressure gas, which is later pressurized to atmospheric pressure and analyzed using a gas chromatograph (GC) (Agilent 7890B) for species concentrations.

The discharge is powered by a nanosecond pulse discharge power supply (Xi'an Lingfengyuan Electronic Technology Co., Ltd., HVP-20P), providing continuous pulse outputs for steady-state gas collection. Each pulse has triangular wave shape with 50 ns rise and fall times, operating at a frequency of 1 kHz and a voltage range of 4.2 kV to 5 kV. Discharge voltage is monitored with a high-voltage probe (Tektronix, P6015A), and discharge current is measured with a current coil (Pearson 6585). Both voltage and current data are recorded using an oscilloscope (Siglent SDS2354X 350 MHz).

2.2. Modelling methods

A new coupled plasma and combustion chemistry solver, CPCC, has been developed by integrating the ZDPlasKin code [23] with a custom-built combustion code in F90 format. CPCC supports sensitivity and path flux analysis and interfaces with popular post-processing software such as Qt-Plaskin [24] and PumpKin [25]. Detailed descriptions of CPCC can be found in [26]. The electron impact process is solved using the Boltzmann equation solver BOLSIG+ [27], which is integrated within ZDPlasKin. The plasma kinetic mechanism and ground state kinetic mechanism are alternately solved

using the splitting method. For efficient solution of large combustion kinetic mechanisms, CPCC utilizes the semi-implicit ODE solver VODPK [28] and the fifth-order implicit Runge-Kutta ODE solver, RADAU5 [29].

The key parameter of the reduced electric field (E/N) is derived from experimental current data using the following equation:

$$I = n_e \mu \left(\frac{E}{N} \right) E e S \quad (1)$$

where n_e is the electron density (initially set to $1.0 \times 10^9 \text{ cm}^{-3}$), I is the electron mobility dependent on the reduced electric field, N is the natural particle density of last time, E is the electric field strength, e is the elementary charge, and S is the cross-sectional area of the plasma. E is iteratively obtained using equation 1 through the Newton iteration method. The initial electron density is given an empirical value, because E is insensitive to the initial electron density, which will iterate consistently to a reasonable value in the first few time steps without affecting the result of the calculation. Then E/N is obtained by dividing E by N .

In present model, as the Poisson equation is not solved, the deposition energy is assumed to be an adjustable parameter and controls the discharge duration [5]. For DBD experiment, the present model's deposition energy stands at $1.85 \times 10^{-5} \text{ cm}^{-3}$, significantly lower than the experimentally measured value. Furthermore, the deposition energy control is not implemented. For nCD experiment, To ensure good agreement with the experimental results, the model utilized 40% of the experimental deposited energy to regulate the discharge time.

To account for primary energy loss due to conduction to the quartz channel walls, similar to the approach in Ref. [7], the model includes surface heat transfer between the plasma and the quartz wall. In the energy equation for the nCD experiment, an additional energy loss term is introduced:

$$\rho C_v \frac{dT_{\text{gas}}}{dt} = - \sum_{i=1}^{i_{\text{max}}} H_i \omega_i - \frac{T_{\text{gas}} - T_{\text{wall}}}{\left(\frac{1}{A_1 h_1} + \frac{\ln(r_2/r_1)}{2\pi\lambda L} \right) V_p} \quad (2)$$

where ρ is the gas density, C_v is the specific heat capacity at constant volume of the gas, H_i and ω_i represent the enthalpy of formation and production/loss rate of component i , respectively. T_{wall} is the outer wall temperature of the quartz tube (set to 300K), A_1 is the contact area between the plasma and

the inner wall of the quartz tube, h_1 is the heat transfer coefficient between the plasma and the inner wall of the quartz tube (which has been adjusted to $10 \text{ W}/(\text{m}^2\text{K})$ based on experimental results due to the cylindrical shape and small diameter of this structure, making empirical formulas unsuitable for estimating the heat transfer coefficient), r_2 and r_1 are the outer and inner radius of the quartz tube, λ is the thermal conductivity of quartz (which is $1.09 \text{ W}/(\text{mK})$), L is the length of the discharge region, and V_p is the volume of the plasma.

For a DBD configuration where the discharge region is rectangular, the energy loss term in the gas energy equation is adjusted as follows:

$$\rho C_v \frac{dT_{\text{gas}}}{dt} = - \sum_{i=1}^{i_{\text{max}}} H_i \omega_i - \frac{T_{\text{gas}} - T_{\text{wall}}}{\left(\frac{1}{A_2 h_2} + \frac{\delta}{A_2 \lambda} \right) V_p} \quad (3)$$

$$h_2 = \frac{\lambda}{LN_u} \quad (4)$$

$$N_u = 0.664 R_e^{1/2} P_r^{1/3} \quad (5)$$

$$P_r = \frac{C_p \mu}{\lambda} \quad (6)$$

$$R_e = \frac{\rho v L}{\mu} \quad (7)$$

where A_2 is the contact area between the plasma and the upper and lower walls, h_2 is the surface heat transfer coefficient of the walls (calculated using equation 4), and the Nusselt number N_u is calculated using equation 5 from the book [30]. P_r is the Prandtl number (calculated by equation 6), R_e is the Reynolds number (calculated by equation 7), μ is the dynamic viscosity, v is the airflow velocity, and C_p is the specific heat capacity at constant pressure of the gas.

This kinetic model includes both plasma chemistry and classical combustion chemistry. The combustion chemistry model incorporates a total of 2521 reactions, which have been updated based on the scheme proposed in Ref. [13]. Specific modifications derived from experimental data are outlined in Table 1. In addition, several combustion reactions have been added and replaced, drawing from various established mechanisms such as HP-Mech v3.3 [31], AramoMech3.0 [32], NUIGMech1.1 [33] (see supplementary material of Table S1). The plasma chemistry model consists of 2202 reactions, involving vibrationally excited species such as $\text{C}_3\text{H}_8(\text{v}1)\text{-C}_3\text{H}_8(\text{v}27)$,

Table 1: Updated plasma reactions and combustion reactions in this work.

Plasma reaction	Original rate constant	Updated rate constant
R1 $e + C_3H_8 \rightarrow e + H_2 + C_3H_6$	$f(\sigma_1)$ [34]	$0.8 \times f(\sigma_1)$
R2 $e + C_3H_8 \rightarrow e + CH_2 + C_2H_6$	$f(\sigma_2)$ [34]	$12 \times f(\sigma_2)$
R3 $e + C_3H_8 \rightarrow e + CH_4 + C_2H_4$	$f(\sigma_3)$ [34]	$0.36 \times f(\sigma_3)$
R4 $e + C_3H_8 \rightarrow e + H_2 + H_2 + C_3H_4$	$f(\sigma_4)$ [34]	$0.75 \times f(\sigma_4)$
R5 $e + C_3H_8 \rightarrow e + CH_2 + C_2H_2 + 2H_2$	0.0	$21 \times f(\sigma_2)$
Combustion reaction	Original Arrhenius equation of A	Updated Arrhenius equation of A
R6 $CH_3OH + O_2 \leftrightarrow CH_3O + HO_2$	3.58×10^4	0.0 [36]
R7 $n-C_3H_7O_2 + HO_2 \leftrightarrow n-C_3H_7O_2H + O_2$	1.75×10^{10}	6.0×10^8
R8 $i-C_3H_7O_2 + HO_2 \leftrightarrow i-C_3H_7O_2H + O_2$	1.75×10^{10}	6.0×10^8
R9 $i-C_3H_7O_2 + C_2H_5O_2 \leftrightarrow CH_3COCH_3 + C_2H_5OH + O_2$	0.0	5.0×10^{16}
R10 $n-C_3H_7O_2 + n-C_3H_7O_2 \leftrightarrow C_2H_5CHO + n-C_3H_7OH + O_2$	1.42×10^{16}	7.0×10^{15}
R11 $n-C_3H_7O_2 + i-C_3H_7O_2 \leftrightarrow C_2H_5CHO + i-C_3H_7OH + O_2$	1.409×10^{16}	4.109×10^{16}
R12 $i-C_3H_7O_2 + n-C_3H_7O_2 \leftrightarrow CH_3COCH_3 + n-C_3H_7OH + O_2$	1.409×10^{16}	1.169×10^{15}
R13 $i-C_3H_7O_2 + i-C_3H_7O_2 \leftrightarrow CH_3COCH_3 + i-C_3H_7OH + O_2$	1.409×10^{16}	2.109×10^{16}

* σ_x indicate the cross sections for the electron-impact reaction. The rate constant values are calculated by BOLSIG+ (indicated by f) given E/N and the cross section data. The unit of cross section data is m^2 . The unit of arrhenius equation pre-exponential factor A is $cm^3 mol^{-1} s^{-1}$.

$CH_4(v2, 4)$, $CH_4(v1, 3)$, $O_2(v1)-O_2(v4)$; electronically excited species like $O_2(a^1\Delta_g)$, $O_2(b^1\Sigma_g^+)$, $O_2(4.5eV)$ (summation of $O_2(c^1\Sigma_u^-)$, $O_2(C^3\Delta_u)$, $O_2(A^3\Sigma_u^+)$), $O(^1D)$, $O(^1S)$, $Ar(1s_2)$, $Ar(1s_4)$, $Ar(11.55eV)$, $Ar(2p_1)$; ions like O^+ , O_2^+ , O^- , O_2^- , O_3^- , CH_4^+ , CH_3^+ , CH_2^+ , CH_5O^+ , $C_2H_3O^+$, CHO_3^- , CO_3^- , CHO_2^- , OH^- , $C_2H_4^+$, $C_2H_5^+$, C_2H^+ , $C_2H_3^+$, $H_5C_2O^+$, $C_3H_7^+$, $C_4H_9^+$, $C_3H_8^+$, and electron. The plasma chemistry model includes chemical reactions involving vibrationally excited states, vibrational relaxation reactions, charge transfer reactions, and reaction channels involving $O(^1D)$, $O(^1S)$, $O_2(a^1\Delta_g)$, $O_2(b^1\Sigma_g^+)$, $O_2(4.5eV)$, $Ar(1s_2)$, $Ar(1s_4)$, $Ar(11.55eV)$, $Ar(2p_1)$ with fuel fragments. The electron collision dissociation cross-section for C_3H_8 is sourced from Ref. [34], while reactions involving electron collision dissociation for CH_4 , including dissociation and ionization, are adopted from Ref. [6]. The plasma chemistry of Ar and O_2 are taken from Ref. [35].

The original model in Section 3 and Section 4 is defined as the plasma chemistry and classical combustion chemistry in which the reaction rate coefficients are from literature without any modifications. Compared to the model of Ref. [13], the original model reconstruct the plasma chemistry and has the same combustion chemistry. As some reactions are not validated with experiments or quantum chemical calculations, the original model predictions for some species have large uncertainties. So the electron impact cross sec-

tions of propane, branch ratios of self-/cross-reactions for i-/n-C₃H₇O₂ and H-abstraction of i-/n-C₃H₇O₂ are fitted within uncertainties according to experimental data and path flux analysis (named as updated model in Section 3 and Section 4). The updated reactions are listed in Table 1. Detailed descriptions and uncertainty analysis can be found in Section 4.1. The species overall predictions of the updated model are highly improved compared to the original model in DBD experiment [13] and nCD experiment conditions. Even so, the quantum chemical calculations or fundamental kinetic experiment are still required to improve the model's prediction capacity.

3. Validation of the mechanism

3.1. Validation I:DBD assisted propane oxidation

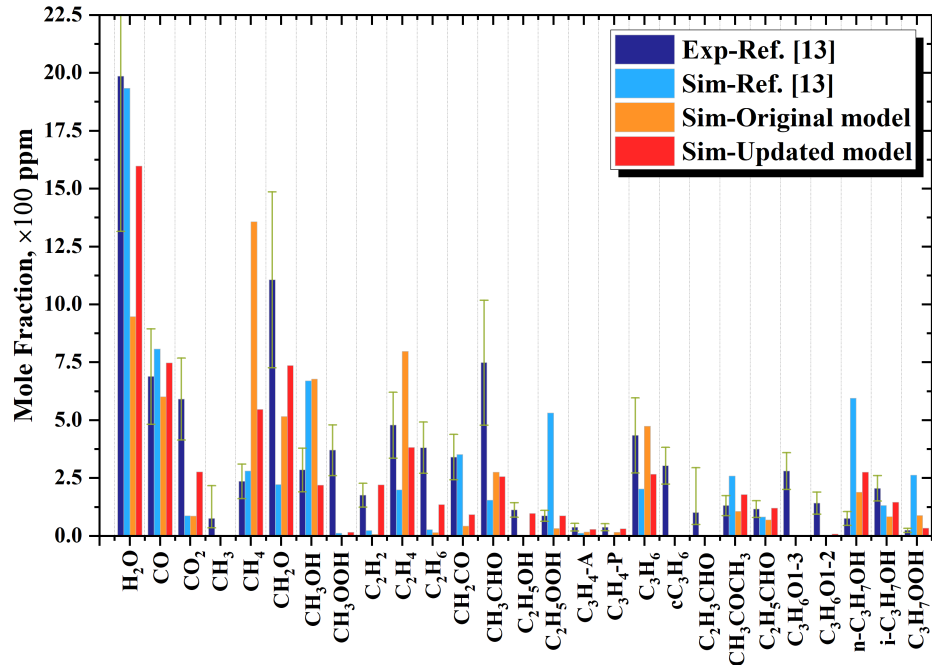


Figure 3: Comparison between measurement and predictions from different kinetics schemes species in repetitively-pulsed nanosecond DBD. The deep blue and light blue bars represent experiment measurement and model prediction results from the Ref. [13].

Model validation is performed by comparing the model predicted and experimental molar fractions of species in a repetitively-pulsed nanosecond

DBD [13], as shown in Fig. 3. The experimental conditions involve a deposition energy of $1.64 \times 10^{-4} J/cm^3$, at 30 Torr and a discharge region temperature of 340 K, with a $C_3H_8/O_2/Ar$ mixture (mole fraction 4:20:76). The updated model's predictions for several species, including H_2O , CO , CH_2O , CH_3OH , C_2H_2 , C_2H_4 , C_2H_5OH , C_2H_5OOH , C_3H_4-A , C_3H_4-P , C_3H_6 , CH_3COCH_3 , C_2H_5CHO , $i-C_3H_7OH$, and C_3H_7OOH are found to be in good agreement with experimental data, falling within the range of experimental measurement errors. The updated model's predictions for species CO_2 , CH_4 , C_2H_6 , CH_2CO , CH_3CHO , and $n-C_3H_7OH$ are within 5 times of the experimental measurement. However, the updated model's predictions for species CH_3 , CH_3OOH , cC_3H_6 , C_2H_3CHO , $C_3H_6O_{1-3}$, and $C_3H_6O_{1-2}$ are over an order of magnitude off. The updated model demonstrates noticeable improvements in prediction accuracy for many species compared to the original model and a previously published model [13].

The reasons for the lower predictions of $C_3H_6O_{1-2}$ and $C_3H_6O_{1-3}$ in the updated model are as follows: In Ref. [37, 38], C_3H_6 is consumed by an O atom to form $C_3H_6O_{1-2}$ and $C_3H_6O_{1-3}$ intermediates through the addition of an O atom to the C=C bonds in the center and end carbon atoms of C_3H_6 . Then, $C_3H_6O_{1-2}$ and $C_3H_6O_{1-3}$ intermediates decompose into CH_3 , C_2H_5 , CH_2O , and H, among others. The reactions provided in Ref. [37] do not consider these intermediate products ($C_3H_6O_{1-2}$ and $C_3H_6O_{1-3}$) but instead directly provide the reactions leading to the final products. This ultimately results in the underprediction of $C_3H_6O_{1-2}$ and $C_3H_6O_{1-3}$.

3.2. Validation II: nCD assisted propane oxidation

The DBD experiment was conducted under conditions with a deposition energy of $1.64 \times 10^{-4} J/cm^3$. To further validate the accuracy of the mechanism, nCD experiments were conducted with deposition energies ranging from $1.7 \times 10^{-4} J/cm^3$ to $1.53 \times 10^{-3} J/cm^3$. The uniformity of the nCD was evaluated using images captured by a high-speed ICCD camera operated at 5.0 kV, which were processed using an Abel transformator, as depicted in Fig. 4. Due to the enhanced electric field near the electrode tip, localized discharge enhancement was observed on the ground electrode. Conversely, a phenomenon of discharge weakening was noted at distances ranging from 9 to 20 mm away from the high-voltage electrode. These localized effects were considered negligible in comparison to the overall discharge characteristics. Overall, the nCD was found to exhibit relatively uniform behavior across the tested conditions.

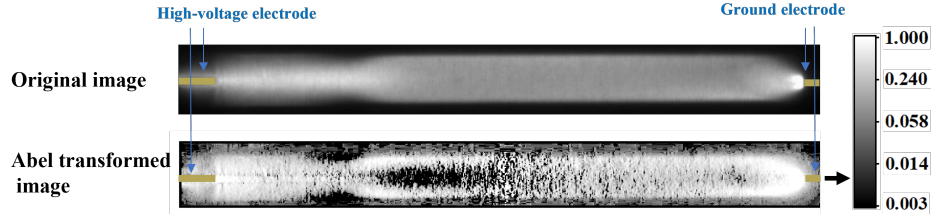


Figure 4: The nCD image captured by high-speed ICCD camera and abel transformed image with voltage of 5.0 kV. The gate width is set to 100ns.

Figure 5 presents a comparison between experimental measurements and predictions from different kinetic schemes in the nCD conditions. The original model exhibits poor predictions for species such as CO, H₂, CO₂, CH₄, C₂H₆, C₂H₂, C₃H₆. In contrast, the updated model shows significant improvements across these species. However, despite these enhancements, notable discrepancies remain in the predicted mole fractions of CO₂, C₂H₄, and CO, which are under-predicted by 55%, 45%, and 45%, respectively.

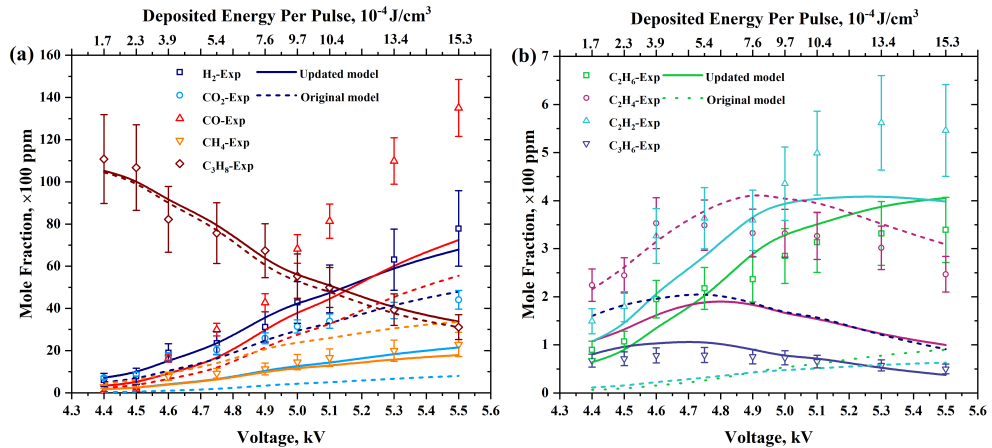


Figure 5: Comparison between measurement and predictions from different kinetics scheme in nCD at different voltages.

The comparison between measurement and predictions from different kinetics scheme in nCD is shown in Fig. 5. The original model has poor predictions in species CO, H₂, CO₂, CH₄, C₂H₆, C₂H₂, C₃H₆. The updated model has great improvement in above mentioned species. However, compared to experimental measurements, the updated model still has significant differences in the mole fractions of CO₂, C₂H₄, and CO. The mole fractions

of updated model are under-predicted by 55%, 45%, and 45%, respectively. The predictions of remaining species are generally well.

The updated model's predictions for C_3H_8 , H_2 , CH_4 , and C_2H_6 generally fall within the experimental error range. For C_3H_6 , while it is overpredicted by 30% at low deposition energy, the agreement improves at higher deposition energies. The trend of C_2H_2 predicted by the updated model aligns with experimental data, albeit with molar fractions approximately 30% lower than measured values. This suggests that while the added reaction pathways in the updated model are correct, further research is needed to refine the cross-sectional data used.

4. Results and discussion

4.1. Uncertain analysis in the plasma and combustion kinetic mechanism

The updated model was derived from the original model through adjustments to several reactions based on experimental findings and pathway flux analysis. Specifically, the modifications listed in Table 1 are discussed in detail as follows.

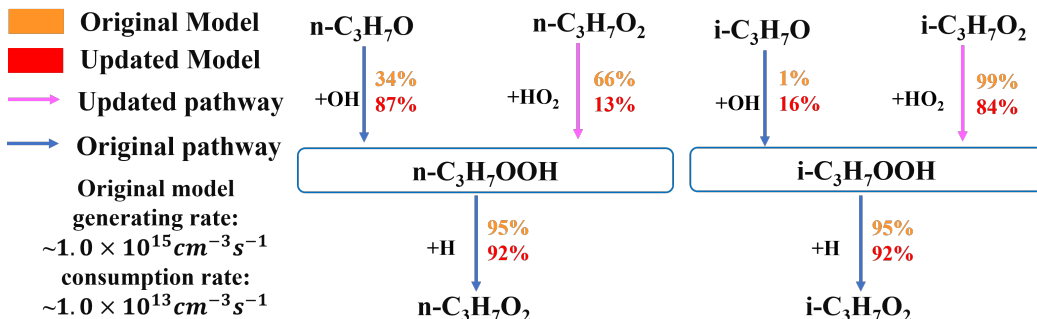


Figure 6: The pathway analysis of i-/n- $\text{C}_3\text{H}_7\text{OOH}$ in the updated model and the original model on the process of DBD assisted propane oxidation.

In the original model, significant over-predictions of i-/n- $\text{C}_3\text{H}_7\text{OOH}$ were observed during the DBD-assisted propane oxidation process, as depicted in Fig. 3. The generation rate of i-/n- $\text{C}_3\text{H}_7\text{OOH}$ was found to be two orders of magnitude larger than its consumption rate. Pathway flux analysis based on the original model identified that the primary generation pathways for i-/n- $\text{C}_3\text{H}_7\text{OOH}$ involved reactions i-/n- $\text{C}_3\text{H}_7\text{O}_2$ with HO_2 (reactions R7 and R8, respectively), as illustrated in Fig. 6. However, the rate coefficients for

R7 and R8 used in the original model were adapted from analogous reactions such as those between CH_3O_2 and HO_2 reported in Ref. [39]. These rate coefficients are valid within a temperature range below 338 K and are subject to an error of up to 5. Given the temperature range of 340-500 K in the current study and the inherent uncertainties associated with the analogy method, significant uncertainties were anticipated for R7 and R8. Therefore, adjustments were made to the rate coefficients of R7 and R8, reducing them by a factor of 0.034 based on insights from the DBD experiment [13]. The updated model now indicates that 87% of $\text{n-C}_3\text{H}_7\text{OOH}$ is generated from the reaction of $\text{n-C}_3\text{H}_7\text{O}$ with OH , while 84% of $\text{i-C}_3\text{H}_7\text{OOH}$ is produced via reaction R8.

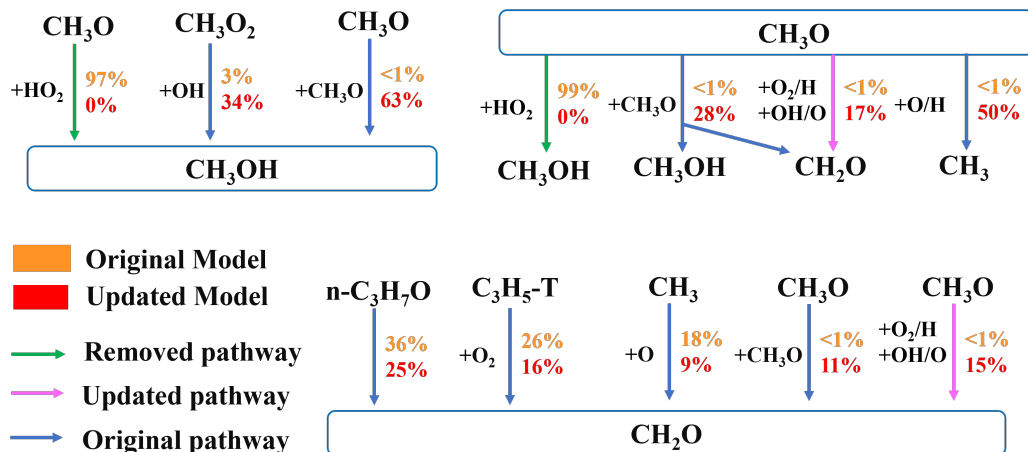
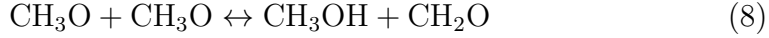


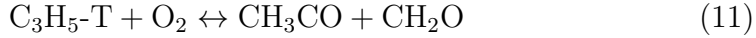
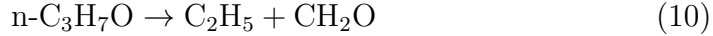
Figure 7: The pathway analysis of CH_3OH , CH_3O and CH_2O in the updated model and the original model on the process of DBD assisted propane oxidation.

Both the model by Chen et al [13] and the original model exhibit under-prediction of CH_2O and over-prediction of CH_3OH . As depicted in Fig. 7, pathway flux analysis of the original model indicates that 97% of CH_3OH is generated via the reaction of CH_3O with HO_2 (R6). However, it was noted that the reaction rate coefficients of R6 were sourced from Ref. [36], which states that the reaction between CH_3OH and O_2 produces CH_2OH and HO_2 , not CH_3O and HO_2 . Consequently, in the updated model, reaction R6 has been removed. The updated model's prediction for CH_3OH now aligns well with experimental measurements, with 63% of CH_3OH being produced by the self-reaction of CH_3O (Reaction 8), and 34% being generated through

Reaction 9.



To address the lack of certain CH_3O consumption pathways, the CH_3O sub-mechanism was supplemented by referencing the HP-Mech v3.3 mechanism [31] (as shown in Table ??). The removal of R6 and the supplement of CH_3O consumption reactions led to significant changes in the CH_3O consumption pathway, as illustrated in Fig. 7. In the original model, CH_3O was almost exclusively consumed by the reverse reaction of R6. In contrast, in the updated model, half of CH_3O is consumed to form CH_3 , while the remaining CH_3O is consumed to form CH_2O and CH_2O . Consequently, the prediction of CH_2O in the updated model has improved and now aligns well with experimental measurements due to the removal of R6 and the supplement of CH_3O consumption reactions.



As depicted in Fig. 3, the original model exhibited over-predictions of $\text{n-C}_3\text{H}_7\text{OH}$ and under-predictions of $\text{i-C}_3\text{H}_7\text{OH}$. It was observed that nearly all $\text{i-C}_3\text{H}_7\text{OH}$ and almost half of $\text{n-C}_3\text{H}_7\text{OH}$ were produced through self- and cross-reactions of $\text{n-}/\text{i-C}_3\text{H}_7\text{O}_2$ (Reactions R10-R13), as illustrated in Fig. 8. The inaccuracies in the branching ratios of these reactions likely contributed to the over-prediction of $\text{n-C}_3\text{H}_7\text{OH}$ and the under-prediction of $\text{i-C}_3\text{H}_7\text{OH}$. The rate coefficients for Reactions R10-R13 were originally derived from Ref. [9]. However, the temperature-dependent rate constants used in Ref. [9], sourced from Ref. [40], lacked detailed pressure and temperature dependencies. Moreover, the products of Reactions R10-R13 were not experimentally validated in Ref. [9], contributing to significant uncertainty in the branch ratios. To improve prediction accuracy, this model adjusted the branching ratios of Reactions R10-R13 based on DBD experimental results. This adjustment notably enhanced the prediction accuracy for $\text{i-C}_3\text{H}_7\text{OH}$,

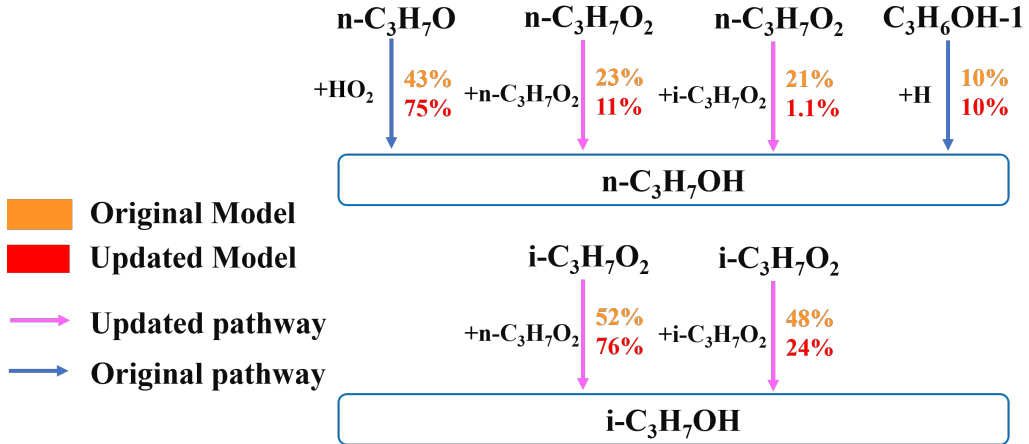


Figure 8: The pathway analysis of $n\text{-C}_3\text{H}_7\text{OH}$ and $i\text{-C}_3\text{H}_7\text{OH}$ in the updated model and the original model on the process of DBD assisted propane oxidation.

although a slight increase in $n\text{-C}_3\text{H}_7\text{OH}$ mole fraction compared to the original model was observed. This increase can be attributed to the enhanced reaction rate of $n\text{-C}_3\text{H}_7\text{O}$ with HO_2 , reflecting the increased mole fraction of HO_2 resulting from the deletion of Reaction R6.

Additionally, a formation pathway for $\text{C}_2\text{H}_5\text{OH}$ was introduced based on the NUIGMech1.1 mechanism [33], using rate coefficients derived from self- and cross-reactions similar to those of $n\text{-}/i\text{-C}_3\text{H}_7\text{O}_2$. This inclusion brought the model's prediction for $\text{C}_2\text{H}_5\text{OH}$ within the experimental measurement error range, as depicted in Fig. 3.

Furthermore, the original model showed under-prediction of $\text{C}_2\text{H}_5\text{OOH}$ compared to experimental measurements, with almost all $\text{C}_2\text{H}_5\text{OOH}$ formed via the reaction between $\text{C}_2\text{H}_5\text{O}_2$ and HO_2 . The increased mole fraction of HO_2 in the updated model led to an enhanced reaction rate between $\text{C}_2\text{H}_5\text{O}_2$ and HO_2 , aligning the predicted mole fraction of $\text{C}_2\text{H}_5\text{OOH}$ more closely with experimental measurements. This further supports the decision to delete Reaction R6.

The discrepancies of CH_4 , C_2H_2 , C_2H_4 , C_2H_6 and C_3H_6 between experimental measurements and the original model are observed in the DBD experiment and the nCD experiment. Given the large energy deposition scales of the nCD experiment, it was chosen as the primary reference for adjusting the kinetic model. A discharge peak voltage of 5.0 kV was selected for pathway flux analysis, as shown in Fig. 9. In the original model, CH_4 , C_2H_4 ,

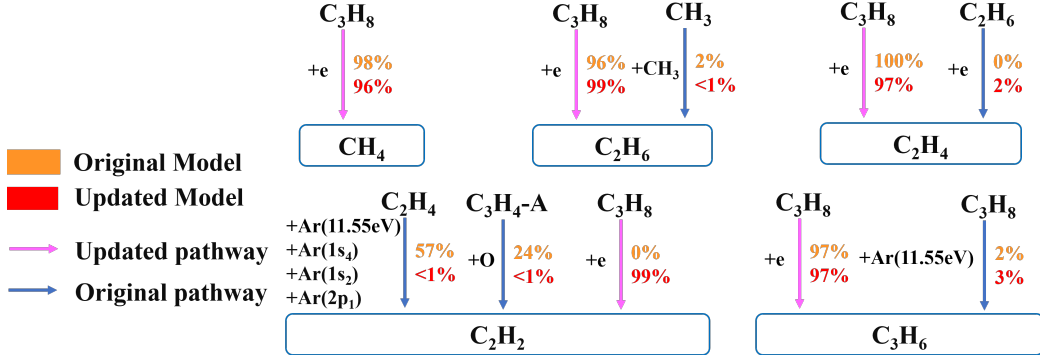


Figure 9: The pathway analysis of CH_4 , C_2H_2 , C_2H_4 , C_2H_6 and C_3H_6 in the updated model and the original model on the process of nCD assisted propane oxidation.

C_2H_6 , and C_3H_6 are produced from the electron impact dissociation of C_3H_8 . The dissociation cross sections for C_3H_8 were obtained from Ref. [34], which provided estimates based on the total experimental dissociation cross sections for both ionized and neutral fragments ($\text{e} + \text{C}_3\text{H}_8 \rightarrow \text{A} + \text{B} + \text{e}$ and $\text{e} + \text{C}_3\text{H}_8 \rightarrow \text{A}^+ + \text{B} + 2\text{e}$). However, the cross-section branch ratios were estimated using empirical formulas, leading to significant uncertainties. Consequently, the reaction rate coefficients for C_3H_8 dissociation were adjusted according to experimental results.

First, in the original model, Reaction (R1) is the primary production pathway for C_3H_6 , and its prediction was overestimated across all discharge voltage scales in the nCD experiment. To improve accuracy, the cross section for Reaction (R1) was reduced by a factor of 0.8, which enhanced the prediction accuracy for C_3H_6 , as shown in Fig. 5.

Second, reaction (R2) is responsible for the formation of C_2H_6 . The original model significantly under-predicted C_2H_6 in the nCD experiment. An adjustment factor of 12 was applied to the cross section for Reaction (R2), aligning the C_2H_6 predictions with the experimental results.

Furthermore, reaction (R3) is the primary pathway for the formation of both CH_4 and C_2H_4 . The plasma sub-mechanism for CH_4 was adopted from Ref. [6, 5] with experimental validation, indicating that the CH_4 consumption rates in the original model were accurate. Despite this, both CH_4 and C_2H_4 were over-predicted in the DBD experiment, and CH_4 was also over-predicted in the nCD experiment. This suggested that the cross section for Reaction (R3) was overestimated. An adjustment to the cross section for Reaction

(R3) was made to achieve better agreement for CH₄ in the nCD experiment and C₂H₄ in the DBD experiment.

Besides, A discrepancy in the prediction of C₃H₄ between the original model and the DBD experiment was noted. Reaction (R4) is responsible for 93% of the formation of C₃H₄-A and C₃H₄-P. Thus, the rate of Reaction (R4) was adjusted to better match the DBD experimental results.

Finally, the original model under-predicted C₂H₂ in both the nCD and DBD experiments, as shown in Fig. 5 and Fig. 3. In the original model, C₂H₂ is generated through reactions between excited argon and C₂H₄ and between O and C₃H₄-A. However, with a mole fraction of C₂H₂ around 600 ppm in the nCD experiment compared to a C₂H₄ mole fraction of less than 400 ppm, C₂H₄ alone cannot account for the C₂H₂ formation. Similarly, C₃H₄-A is present at too low a concentration to significantly contribute to C₂H₂ production. Therefore, electron-impact dissociation of C₃H₈ (Reaction R5) was considered as a primary source for C₂H₂. Adding Reaction (R5) to the updated model significantly improved the accuracy of C₂H₂ predictions, with the updated model's C₂H₂ predictions closely matching experimental results from both the nCD and DBD experiments.

As stated above, The model undergoes significant updates through pathway flux analysis informed by experiments conducted under nCD and DBD conditions. By adjusting key reaction mechanisms according to experimental data, including C₃H₆, C₂H₆, CH₄, C₂H₄, C₂H₂, and C₃H₄, the updated model now demonstrates markedly improved predictive accuracy. This enhancement is particularly evident in its ability to better replicate experimental observations in both nCD and DBD experiments.

4.2. The comparisons of C₃H₈ oxidation process assisted by DBD and nCD

To explore the impact of the single pulse deposition energy (SPDE) on the oxidation of C₃H₈, we have designed three distinct cases, each tailored to mimic specific energy deposition conditions. As depicted in Table 2, these cases are denoted as Case1, Case2, and Case3, with corresponding SPDE values in the model set at $1.85 \times 10^{-5} \text{ J/cm}^3$, $9.08 \times 10^{-5} \text{ J/cm}^3$, and $3.9 \times 10^{-4} \text{ J/cm}^3$, respectively. Notably, the total deposition energy in the model is standardized at $7.36 \times 10^{-3} \text{ J/cm}^3$ by adjusting the discharge frequency and pulse number, ensuring consistency across the cases. Furthermore, the gas temperature is maintained at a constant 400 K, while the discharge current values for the DBD and nCD in the models are sourced from Ref. [13] and the nCD experiment, respectively. These cases are designed to provide insights

into the role of SPDE on C_3H_8 oxidation, offering valuable comparisons under varying energy deposition conditions.

Table 2: Initial parameters of simulation cases.

	Case1	Case2	Case3
Discharge type	DBD	nCD	nCD
Peak voltage, kV	9.0	4.5	5.0
Discharge time, ms		20	
Frequency, Hz	20000	4050	950
Pulse number	400	81	19
Single pulse deposition energy in model, J/cm^3	1.85×10^{-5}	9.08×10^{-5}	3.9×10^{-4}
Total deposition energy in model, J/cm^3		7.36×10^{-3}	
Gas temperature, K		400	
Pressure, Pa		4000	
Discharge mixture	$\text{C}_3\text{H}_8/\text{O}_2/\text{Ar}$ 4:20:76		

In Fig. 10(a), the average reduced electric field evolution for DBD and nCD is depicted, where the reduced electric field is averaged over all discharge pulses. Notably, the average reduced electric field for nCD experiences a rapid increase to 450-500 Td before 3 ns, followed by a dramatic decrease to 150-200 Td at 8 ns, maintaining this level until the end of the discharge. In contrast, the average reduced electric field for DBD fluctuates repeatedly from 0 Td to 400 Td. As illustrated in Fig. 10(b), the reduced electric field distribution for nCD is concentrated at 150-200 Td and 450-500 Td. In comparison, the reduced electric field distribution for DBD predominantly ranges from 0-25 Td and 50-250 Td, accounting for approximately 55% and 35%, respectively, indicating a lower reduced electric field distribution compared to nCD.

Fig. 11 presents a comparison of species density in the C_3H_8 oxidation process assisted by DBD and nCD. Interestingly, the density of species such as H_2O , CO , CO_2 , C_2H_2 , and C_2H_4 in the C_3H_8 oxidation process remains similar between DBD and nCD, despite varying SPDE values. This suggests that SPDE has minimal influence on the C_3H_8 oxidation process when the total deposition energy remains constant. Furthermore, Fig. 12 highlights the time evolution of C_3H_6 and CH_4 in the C_3H_8 oxidation process assisted by DBD and nCD. Both C_3H_6 and CH_4 are produced during nanosecond pulse discharge and subsequently consumed in the discharge gaps. Notably, the increase in C_3H_6 and CH_4 during a given period correlates with the rise in SPDE. These observations collectively suggest that the C_3H_8 oxidation process is primarily controlled by total deposition energy and displays limited

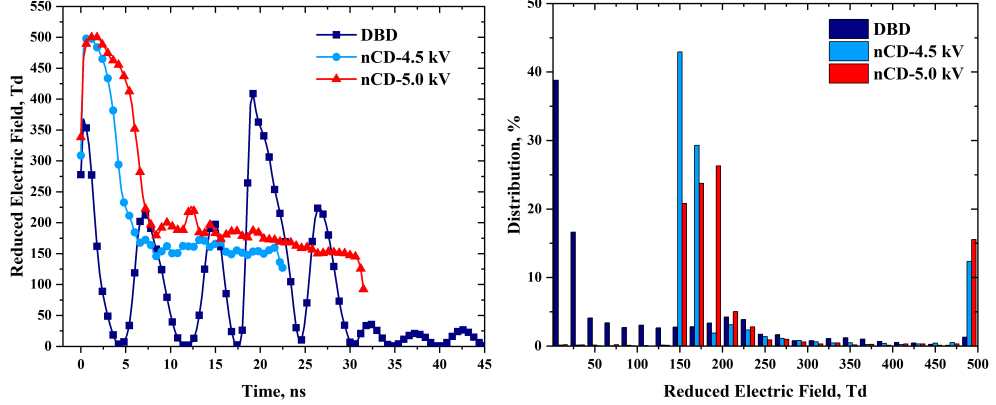


Figure 10: The comparison of average reduced electric field and reduced electric field distribution in DBD and nCD.

correlation with the specific discharge type, be it DBD or nCD.

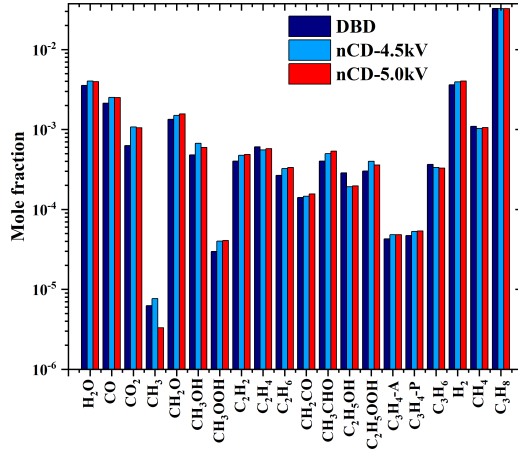


Figure 11: Comparison of species density in C_3H_8 oxidation process assisted by DBD and nCD.

As depicted in Fig. 13, the consumption pathways of C_3H_8 in DBD and nCD environments were analyzed. In DBD, 57% of C_3H_8 is consumed through vibrationally excited reactions, attributed to the concentrated reduced electric field distribution of 0-25 Td, which enhances efficient vibrational excitation. Conversely, in nCD, a lower proportion of C_3H_8 is consumed via vibrationally excited reactions, with a higher contribution from species such as $\text{O}({}^1\text{D})$, Ar^+ , e , and OH . $\text{C}_3\text{H}_8(\text{v})$ is quenched back to C_3H_8

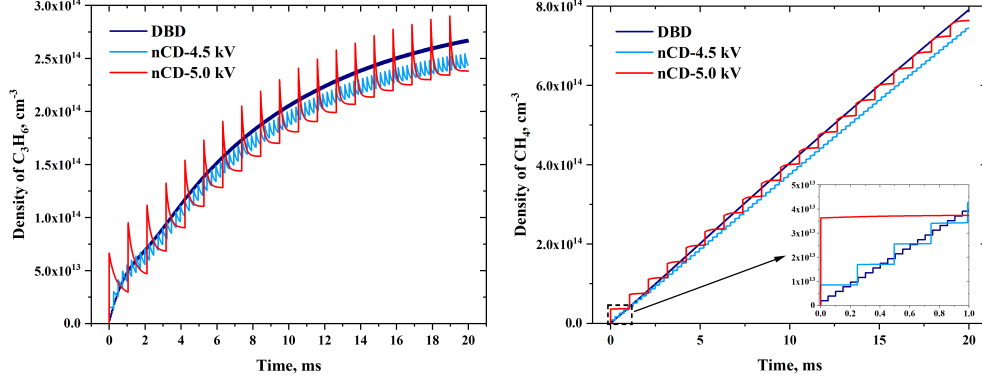


Figure 12: C_3H_6 and CH_4 time evolutions in C_3H_8 oxidation process assisted by DBD and nCD.

through relaxation reactions, contributing thermally to the process. Although a significant portion of C_3H_8 in DBD is excited to $\text{C}_3\text{H}_8(v)$, the energy deposited into $\text{C}_3\text{H}_8(v)$ remains relatively low due to the limited vibrational excitation energy. In DBD, the majority of energy deposition occurs within the 100-250 Td range, similar to processes occurring at 150-200 Td and 500 Td in nCD. Consequently, the species density in the C_3H_8 oxidation process, whether assisted by DBD or nCD, exhibits comparable values. Additionally, the time evolutions of C_3H_6 and CH_4 densities in both nCD and DBD environments display similar tendencies.

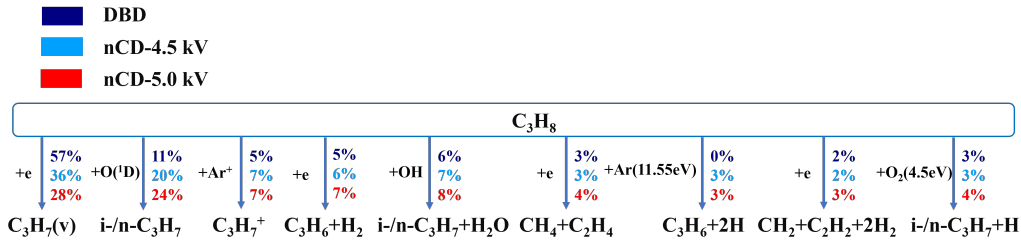


Figure 13: C_3H_8 consumption pathways analysis in DBD and nCD.

5. Conclusions

This study investigates the kinetics of plasma-assisted propane oxidation in nanosecond pulse discharge. A zero-dimensional plasma-combustion

coupled solver equipped with sensitivity and pathway flux analysis modules was developed, based on the ZDPlaskin package and a custom-built combustion chemistry code. A kinetic model was proposed and validated against the nCD experiment using gas chromatography and the nanosecond DBD experiment using synchrotron photoionization mass spectrometry. The updated model demonstrates predictions for 15 species falling within the range of DBD experimental measurement errors, with significantly improved prediction accuracy for 17 species. Notably, the updated model exhibits good prediction accuracy with the nCD experiment for C₃H₈, H₂, CH₄, and C₂H₆ under large deposition energy scales. However, the model-predicted fractions of CO₂, C₂H₄, and CO are 55%, 45%, and 45% lower than those measured in the nCD experiment, respectively.

Several modifications to the reactions were made based on experiments and pathway flux analysis. This included fitting the reaction rate coefficients of i-/n-C₃H₇O₂ with HO₂ (R7, R8) due to the large uncertainty of the analogy method. Additionally, the deletion of the erroneous addition reaction CH₃OH + O₂ \leftrightarrow CH₃O + HO₂ resulted in improved model predictions for CH₃OH. The supplementation of the CH₃O sub-mechanism from the HP-Mech v3.3 mechanism enhanced the updated model's prediction accuracy for CH₂O. Furthermore, adjustments to the C₃H₈ dissociation reaction rate coefficients, owing to large uncertainties, greatly improved the prediction accuracy for H₂, CH₄, C₂H₆, C₂H₂, and C₃H₆.

Comparisons of C₃H₈ oxidation processes assisted by DBD and nCD under varying SPDE but with the same total deposition energy revealed that the process is primarily controlled by total deposition energy, demonstrating minimal influence from SPDE and displaying limited correlation with the specific discharge types, DBD and nCD.

Overall, these findings illustrated the intricate interplay between plasma and combustion chemistry, offering valuable insights into the mechanisms of plasma-assisted propane oxidation.

Acknowledgments

The work is supported by the National Natural Science Foundation of China (No.52277168, No.52025064, No.52207151), the National Key Research and Development Program of China (No.2023YFB4005700, No.2023YFB4005705, and No.2023YFB4005702-03), the University Synergy Innovation Program of Anhui Province (No.GXXT-2022025), and the independent project of the

Energy Research Institute of Hefei Comprehensive National Science Center (Anhui Energy Laboratory) (No.22KZZ525, No.23KZS402, No.22KZS301, and No.22KZS304). The authors are thankful to the young research group in Atelier des Plasmas for fruitful discussions.

References

- [1] Y. Ju, W. Sun, Plasma assisted combustion: Dynamics and chemistry, PROG ENERG COMBUST 48 (2015) 21–83.
- [2] Y. Ju, J. K. Lefkowitz, C. B. Reuter, S. H. Won, X. Yang, S. Yang, W. Sun, Z. Jiang, Q. Chen, Plasma assisted low temperature combustion, PLASMA CHEM PLASMA P 36 (2016) 85–105.
- [3] A. Starikovskiy, N. Aleksandrov, Plasma-assisted ignition and combustion, PROG ENERG COMBUST 39 (2013) 61–110.
- [4] X. Mao, Q. Chen, Effects of vibrational excitation on nanosecond discharge enhanced methane–air ignition, AIAA J 56 (2018) 4312–4320.
- [5] X. Mao, Q. Chen, C. Guo, Methane pyrolysis with n2/ar/he diluents in a repetitively-pulsed nanosecond discharge: Kinetics development for plasma assisted combustion and fuel reforming, ENERG CONVERS MANAGE 200 (2019) 112018.
- [6] X. Mao, A. Rousso, Q. Chen, Y. Ju, Numerical modeling of ignition enhancement of ch4/o2/he mixtures using a hybrid repetitive nanosecond and dc discharge, P COMBUST INST 37 (2019) 5545–5552.
- [7] J. K. Lefkowitz, P. Guo, A. Rousso, Y. Ju, Species and temperature measurements of methane oxidation in a nanosecond repetitively pulsed discharge, PHILOS T ROY SOC A 373 (2015) 20140333.
- [8] J. Sun, Q. Chen, B. Zhao, C. Guo, J. Liu, M. Zhang, D. Li, Temperature-dependent ion chemistry in nanosecond discharge plasma-assisted ch4 oxidation, J PHYS D APPL PHYS 55 (2022) 135203.
- [9] O. Welz, M. P. Burke, I. O. Antonov, C. F. Goldsmith, J. D. Savee, D. L. Osborn, C. A. Taatjes, S. J. Klippenstein, L. Sheps, New insights into low-temperature oxidation of propane from synchrotron photoionization

mass spectrometry and multiscale informatics modeling, *J PHYS CHEM A* 119 (2015) 7116–7129.

- [10] S. S. Merchant, C. F. Goldsmith, A. G. Vandeputte, M. P. Burke, S. J. Klippenstein, W. H. Green, Understanding low-temperature first-stage ignition delay: Propane, *COMBUST FLAME* 162 (2015) 3658–3673.
- [11] I. V. Adamovich, T. Li, W. R. Lempert, Kinetic mechanism of molecular energy transfer and chemical reactions in low-temperature air-fuel plasmas, *PHILOS T ROY SOC A* 373 (2015) 20140336.
- [12] Z. Eckert, N. Tsolas, K. Togai, A. Chernukho, R. A. Yetter, I. V. Adamovich, Kinetics of plasma-assisted oxidation of highly diluted hydrocarbon mixtures excited by a repetitive nanosecond pulse discharge, *J PHYS D APPL PHYS* 51 (2018) 374002.
- [13] H. Chen, R. Zhang, H. Liao, F. Zhang, J. Yang, B. Yang, Kinetic insights into plasma-assisted low-temperature oxidation of propane with synchrotron photoionization mass spectrometry, *P COMBUST INST* 39 (2023) 5499–5509.
- [14] Y. Ban, S. Zhong, J. Zhu, F. Zhang, Effects of non-equilibrium plasma and equilibrium discharge on low-temperature combustion in lean propane/air mixtures, *Fuel* 339 (2023) 127353.
- [15] L. Wu, J. Lane, N. Cernansky, D. Miller, A. Fridman, A. Y. Starikovskiy, Plasma-assisted ignition below self-ignition threshold in methane, ethane, propane and butane-air mixtures, *P COMBUST INST* 33 (2011) 3219–3224.
- [16] Y. Akishev, T. Alekseeva, V. Karalnik, A. Petryakov, On the slow ionization waves forming the breakdown in a long capillary tube with helium at low pressure, *J PHYS D APPL PHYS* 55 (2022) 145202.
- [17] A. Klochko, A. Salmon, J. Lemainque, N. Popov, S. Starikovskaia, Capillary nanosecond discharges as a tool for the measurement of quenching coefficients at high specific energy deposition, in: 53rd AIAA Aerospace Sciences Meeting, 2015, p. 0937.
- [18] T. L. Chng, I. Orel, S. Starikovskaia, I. Adamovich, Electric field induced second harmonic (e-fish) generation for characterization of fast

ionization wave discharges at moderate and low pressures, PLASMA SOURCES SCI T 28 (2019) 045004.

- [19] A. Klochko, A. Salmon, N. Popov, J.-P. Booth, M. J. Kushner, Z. Xiong, S. Starikovskaya, Experimental and numerical study of fast gas heating and o atom production in a capillary nanosecond discharge, in: 52nd Aerospace Sciences Meeting, 2014, p. 1030.
- [20] N. Lepikhin, A. Klochko, N. Popov, S. Starikovskaya, Long-lived plasma and fast quenching of n2 (c3πu) by electrons in the afterglow of a nanosecond capillary discharge in nitrogen, PLASMA SOURCES SCI T 25 (2016) 045003.
- [21] X. Chen, Y. Zhu, Y. Wu, J. Hao, X. Ma, P. Lu, Modeling of fast ionization waves in pure nitrogen at moderate pressure, PLASMA SOURCES SCI T 30 (2021) 065002.
- [22] Y. Zhu, S. M. Starikovskaya, N. Y. Babaeva, M. J. Kushner, Scaling of pulsed nanosecond capillary plasmas at different specific energy deposition, PLASMA SOURCES SCI T 29 (2020) 125006.
- [23] S. Pancheshnyi, B. Eismann, G. Hagelaar, L. Pitchford, Computer code zdplaskin, University of Toulouse, LAPLACE, CNRS-UPS-INP, Toulouse, France (2008). URL: <http://www.zdplaskin.laplace.univ-tlse.fr>.
- [24] A. Luque, Qtplaskin, the Instituto de Astrofísica de Andalucía (IAA) (2020). URL: <https://github.com/aluque/qtplaskin/>.
- [25] A. H. Markosyan, A. Luque, F. J. Gordillo-Vázquez, U. Ebert, Pumpkin: A tool to find principal pathways in plasma chemical models, Computer Physics Communications 185 (2014) 2697–2702.
- [26] Y. Qiu, Y. Zhu, Y. Wu, N. Zhao, Z. Li, M. Hao, B. Zhang, D. Pan, Numerical investigation of the hybrid pulse–dc plasma assisted ignition and nox emission of nh3/n2/o2 mixture, COMBUST FLAME 258 (2023) 113078.
- [27] G. Hagelaar, L. C. Pitchford, Solving the boltzmann equation to obtain electron transport coefficients and rate coefficients for fluid models, PLASMA SOURCES SCI T 14 (2005) 722.

- [28] A. C. Hindmarsh, Odepack, a systemized collection of ode solvers, *Scientific computing* (1983).
- [29] N. Guglielmi, E. Hairer, Implementing radau iia methods for stiff delay differential equations, *Computing* 67 (2001) 1–12.
- [30] S. Yang, W. Tao, *Chuan re xue[Heat transfer theory]*, Higher Education Press, 2006.
- [31] C. B. Reuter, R. Zhang, O. R. Yehia, Y. Rezgui, Y. Ju, Counterflow flame experiments and chemical kinetic modeling of dimethyl ether/methane mixtures, *COMBUST FLAME* 196 (2018) 1–10.
- [32] C.-W. Zhou, Y. Li, U. Burke, C. Banyon, K. P. Somers, S. Ding, S. Khan, J. W. Hargis, T. Sikes, O. Mathieu, et al., An experimental and chemical kinetic modeling study of 1, 3-butadiene combustion: Ignition delay time and laminar flame speed measurements, *COMBUST FLAME* 197 (2018) 423–438.
- [33] A. Ramalingam, S. Panigrahy, Y. Fenard, H. Curran, K. A. Heufer, A chemical kinetic perspective on the low-temperature oxidation of propane/propene mixtures through experiments and kinetic analyses, *COMBUST FLAME* 223 (2021) 361–375.
- [34] R. K. Janev, D. Reiter, Collision processes of hydrocarbon species in hydrogen plasmas: II. The ethane and propane families, *Forschungszentrum, Zentralbibliothek*, 2002.
- [35] Y. Zhu, N. D. Lepikhin, I. S. Orel, A. Salmon, A. V. Klochko, S. M. Starikovskaia, Optical actinometry of o-atoms in pulsed nanosecond capillary discharge: peculiarities of kinetics at high specific deposited energy, *PLASMA SOURCES SCI T* 27 (2018) 075020.
- [36] S. J. Klippenstein, L. B. Harding, M. J. Davis, A. S. Tomlin, R. T. Skodje, Uncertainty driven theoretical kinetics studies for ch3oh ignition: Ho2+ ch3oh and o2+ ch3oh, *P COMBUST INST* 33 (2011) 351–357.
- [37] Y. Bedjanian, J. Morin, Reaction of o (3p) with c3h6: Yield of the reaction products as a function of temperature, *J PHYS CHEM A* 121 (2017) 1553–1562.

- [38] F. Leonori, N. Balucani, V. Nevrly, A. Bergeat, S. Falcinelli, G. Vanuzzo, P. Casavecchia, C. Cavallotti, Experimental and theoretical studies on the dynamics of the $\text{O} (3p) +$ propene reaction: primary products, branching ratios, and role of intersystem crossing, *J PHYS CHEM C* 119 (2015) 14632–14652.
- [39] W. Tsang, Chemical kinetic data base for combustion chemistry. part 2. methanol, *J PHYS CHEM REF DATA* 16 (1987) 471–508.
- [40] R. Atkinson, D. Baulch, R. Cox, J. Crowley, R. Hampson, R. Hynes, M. Jenkin, M. Rossi, J. Troe, I. Subcommittee, Evaluated kinetic and photochemical data for atmospheric chemistry: Volume ii—gas phase reactions of organic species, *ATMOS CHEM PHYS* 6 (2006) 3625–4055.